Stellar Atmospheric Parameters of M-type Stars from LAMOST DR8

Ming-Yi Ding[1,2] , Jian-Rong Shi[1,2] , Yue Wu[1], Hugh R. A. Jones[3] , Hong-Liang Yan[1,2] , Chun-Qian Li[1,2] , Qi Gao[1,2] ,
Tian-Yi Chen[1,2] , Jing-Hua Zhang[1] , Shuai Liu[1,2] , Tai-Sheng Yan[1,2] , and Xiao-Jin Xie[1,4]

[1] CAS Key Laboratory of Optical Astronomy, National Astronomical Observatories, Chinese Academy of Sciences, Beijing 100101, People's Republic of China
sjr@nao.cas.cn, hlyan@nao.cas.cn
[2] School of Astronomy and Space Science, University of Chinese Academy of Sciences, Beijing 100049, People's Republic of China
[3] Centre for Astrophysics Research, University of Hertfordshire, College Lane, AL10 9AB, Hatfield, UK
[4] Tibet University, Lhasa 850000, People's Republic of China

Abstract

The Large Sky Area Multi-Object Fiber Spectroscopic Telescope (LAMOST) Low Resolution Spectroscopic Survey (LRS) provides massive spectroscopic data on M-type stars, and the derived stellar parameters could bring vital help to various studies. We adopt the ULySS package to perform χ^2 minimization with model spectra generated from the MILES interpolator and determine the stellar atmospheric parameters for the M-type stars from LAMOST LRS Data Release 8. Comparison with the stellar parameters from the APOGEE Stellar Parameter and Chemical Abundance Pipeline (ASPCAP) suggests that most of our results have good consistency. For M dwarfs, we achieve dispersions better than 74 K, 0.19 dex, and 0.16 dex for $T_{\rm eff}$, $\log g$, and [Fe/H], while for M giants, the internal uncertainties are 58 K, 0.32 dex, and 0.26 dex, respectively. Compared to ASPCAP we also find a systematic underestimation of $\Delta T_{\rm eff} = -176$ K for M dwarfs and a systematic overestimation of $\Delta \log g = 0.30$ dex for M giants. However, such differences are less significant when we make a comparison with common stars from other literature, which indicates that systematic biases exist in the difference between ASPCAP and other measurements. A catalog of 763,136 spectra corresponding to 616,314 M-type stars with derived stellar parameters is presented. We determine the stellar parameters for stars with $T_{\rm eff}$ higher than 2900 K, with $\log g$ from -0.24 dex to 5.9 dex. The typical precisions are 45 K, 0.25 dex, and 0.22 dex, for $T_{\rm eff}$, $\log g$, and [Fe/H], respectively, which are estimated from duplicate observations of the same stars.

1. Introduction

Of the adopted astronomical spectral types, the M spectral type shows the most wide-ranging properties. On the Hertzsprung–Russell (H-R) diagram, the M dwarfs (dMs) and the M giants (gMs) showed the most extreme differences in luminosity and radius (e.g., Gray & Corbally 2009). The dMs are the faintest of the core hydrogen burners (e.g., Kirkpatrick 1992), while the gMs might have the largest brightness variations. Studies of low-mass main-sequence dMs show that dMs are the most common stars in the Galaxy, which comprise 70% of all stars (e.g., Laughlin et al. 1997). The dMs are very important to determine the initial mass function, which constrains theoretical star formation studies, and they are helpful in tracing the chemical and dynamical history of the Galaxy.

The main-sequence types—O, B, A, F, G, and K stars—are considered to be completely hydrogen-burning stars, while the later-type (giant—S and C types, dwarf—L, T, and Y types) stars appear more likely to be carbon stars or brown dwarfs (Kirkpatrick et al. 1999). The turning point for these later spectral types is the M-type stars, and they are a milestone in the study of the chemical and dynamical evolution of the Galaxy.

M-type stars are iconic for their crowded molecular absorption bands (Gray & Corbally 2009), making their continuum difficult to define in the optical region. Over the years, methods based on the measurement of the atomic and molecular features in the optical and near-infrared region (6300–9000 Å), such as the use of TiO, CaH, and Ca II triplet, are highlighted in stellar atmospheric parameter determination for M-type stars (Bessell 1991; Kirkpatrick 1992; Reid et al. 1995; Cenarro et al. 2001, etc.). In a work on M-subdwarf (sdM) classification, Gizis (1997) showed the metallicity dependency on the TiO and CaH features in the region of 6200 to 7400 Å.

Likewise, an empirical spectroscopic index has been suggested (Lepine et al. 2007) for sdM classification, which is defined as the relative strength of TiO5 and CaH molecular absorption bands. Mann et al. (2012) used six different gravity-sensitive molecular and atomic indices to determine the luminosity class for late-type Kepler exoplanet candidates. The spectral index of TiO5 and CaH2+CaH3 was used to separate dMs from gMs and sdMs in Large Sky Area Multi-Object Fiber Spectroscopic Telescope (LAMOST) Data Release (DR) 1 (Luo et al. 2015) and to assemble these stars into an M-type spectral template library (Zhong et al. 2015a, 2015b). By employing this template, Zhang et al. (2019) calibrated the spectroscopic index and applied a new separator to identify 2791 new sdMs from LAMOST DR4.

Currently, thanks to several ongoing large-scale spectroscopic surveys, large numbers of spectra along with stellar parameters are available now. For example, the Sloan Digital Sky Survey (SDSS) uses the Sloan Foundation 2.5 m telescope

at Apache Point Observatory (Gunn et al. 2006) to determine spectroscopic abundances on a large scale. The Apache Point Observatory Galactic Evolution Experiment (APOGEE, Majewski et al. 2017) is one of the subprojects of SDSS-III (Eisenstein et al. 2011), which provides high-resolution ($R \sim 22,500$), high signal-to-noise ratio (S/N > 100), near-infrared spectra. During the second generation of the APOGEE project (APOGEE-2) with SDSS-IV, the latest DR17 presents spectra for about 650,000 stars. Meanwhile, a set of stellar parameters and chemical abundances of up to 26 elements is also provided through the APOGEE Stellar Parameter and Chemical Abundances Pipeline (ASPCAP; García Pérez et al. 2016), which fits the observed spectra via comparison to the synthetic spectra generated from the MARCS stellar atmospheric model. Jönsson et al. (2020) updated ASPCAP with the precalculated grids (Gustafsson et al. 2008), which improved the model performance under the effective temperature of 3500 K, and made the stellar parameters for cool stars more accurate compared to the previous version. Other spectroscopic surveys, such as LAMOST (Cui et al. 2012), the Radial Velocity Experiment (RAVE; Steinmetz et al. 2006), the Galactic Archaeology with HERMES (GALAH; De Silva et al. 2015), Gaia-ESO (Brown et al. 2018), and the Calar Alto high-Resolution search for M dwarfs with Exo-earths with Near-infrared and optical Echelle Spectrographs (CARMENES; Reiners et al. 2018; Quirrenbach et al. 2020), also provide relevant large-scale spectroscopic data of M-type stars.

In stellar astrophysics research, stellar atmospheric parameters (effective temperature $T_{\rm eff}$, surface gravity $\log g$, and metallicity [Fe/H]) derived from high-resolution and high-S/N spectra are important indicators. During the past few years, different methods have been developed to determine the stellar parameters from high-quality spectra. Generally, these approaches could be simply divided into two categories (Wu et al. 2011); the first one is the minimum distance method (MDM), including the measurement of equivalent width (EWs) or synthetic spectra based on absorption lines (Jofré et al. 2019). For example, the χ^2 minimization is a widely used MDM method, which searches for the minimum χ^2 between the observed spectra and the templates or spectra generated from stellar atmospheric models. The other one is so-called machine-learning approaches, such as the artificial neural network (ANN) and nonlinear regression methods.

Mann et al. (2015) determined the precise stellar parameters for 183 nearby dMs via the MDM method and presented empirical relations between $T_{\rm eff}$, absolute magnitude, radius, mass, and bolometric flux. In a search for exoplanets around dMs, Passegger et al. (2018) determined the stellar atmospheric parameters for over 300 dMs by fitting the spectra generated from the PHOENIX-ACES (Husser et al. 2013) models. Rajpurohit et al. (2018) determined the stellar parameters for 292 early to late M-type stars by comparing high-resolution spectra with the synthetic spectra obtained from BT-Settl (Allard et al. 2011, 2012, 2013). This model is also used to derive the stellar atmospheric parameters and kinematics for sdMs from the LAMOST survey by Zhang et al. (2021).

Similarly, Kesseli et al. (2019) obtained $T_{\rm eff}$ for 88 sdMs using the BT-Settl grid and [Fe/H] values estimated from the color empirical relation (Newton et al. 2014). Hejazi et al. (2020) presented a catalog of 1544 nearby dMs with stellar parameters determined from the latest version of the BT-Settl model. Sarmento et al. (2021) derived the stellar parameters for

313 dMs through χ^2 minimization using APOGEE H-band spectra. The LAMOST Stellar Parameter Pipeline at Peking University (LSP3) adopts a cross-correlation algorithm to determine stellar radial velocities (RV) and uses a template-matching method for stellar atmospheric parameter determination (Xiang et al. 2015).

Machine-learning methods make stellar parameter predictions based on data-driven models learned from a large data set. The advantage of these data-driven models is their flexibility in learning patterns from spectra and transforming them into various stellar parameters. Maldonado et al. (2020) presented a catalog of $T_{\rm eff}$ and [Fe/H] via principal component analysis (PCA) and sparse Bayesian methods for 204 dMs from the HARPS GTO M-dwarf survey (Bonfils et al. 2013). Based on The Cannon (Ness et al. 2015; Casey et al. 2016; Ho et al. 2017), Birky et al. (2020) trained a data-driven model with high-resolution spectra from APOGEE and derived stellar parameters ($T_{\rm eff}$ and [Fe/H]) for 5875 M-type stars. Passegger et al. (2020) trained a convolutional neural network (CNN) based on synthetic spectra generated from the PHOENIX-ACES model to estimate the stellar parameters for CAR-MENES dMs.

The Stellar Parameters and Chemical Abundances Network (SPCANet; Wang et al. 2020) constructed a CNN with three convolutional layers trained on spectra from the LAMOST Medium Resolution Spectroscopic survey (MRS; Liu et al. 2020) with the APOGEE Payne (Ting et al. 2019) stellar labels. Based on the support vector regression (SVR; Smola & Schölkopf 2004) method, Zhang et al. (2020) developed a data-driven approach called the Stellar Label Machine (SLAM), which performs a nonlinear regression on stellar labels and the spectrum itself, and estimated the stellar labels for stars from LAMOST DR5 over a wide range of spectral types. Li et al. (2021) adapted the SLAM program by introducing the APOGEE stellar labels and synthetic spectra from the BT-Settl model as training sets and obtained the stellar parameters for dMs from LAMOST DR6.

The empirical spectral library is also commonly used for determining the stellar parameters in large-scale spectroscopic surveys, which directly or indirectly compare the observed spectra with templates listed in the spectral library. Yee et al. (2017) presented a high-resolution, high-S/N empirical spectral library of 76 dMs, along with the parameterizing tool "Empirical SpecMatch," which estimates the stellar parameters for FGKM stars by comparing them against this spectral library. Other empirical spectral libraries, including STELIB (Le Borgne et al. 2003), ELODIE (Prugniel & Soubiran 2001; Prugniel et al. 2007), CFLIB (Indo-US library) (Valdes et al. 2004), and MILES (Sanchez-Blazquez et al. 2006; Falcón-Barroso et al. 2011), are composed of high-quality spectra with good coverage of stellar atmospheric parameter space. With the help of empirical libraries of homogeneous M-type star templates, we are able to derive precise stellar atmospheric parameters by matching our spectra to these templates.

In this study, we employ the ULySS (Koleva et al. 2009) package to perform χ^2 minimization between the observed and model spectra and use the MILES interpolator (Sharma et al. 2016) to estimate the stellar atmospheric parameters for M-type stars from the LAMOST Low Resolution Spectroscopic survey (LRS) DR8.

The structure of this paper is as follows. Section 2 introduces the preparation of our spectra from the LAMOST survey, and

Section 3 gives a brief description of the interpolation model and the ULySS program. In Section 4, we present the summary of our results and compare the stellar parameters derived from our method with those in the literature. The deviation and precision are discussed in Section 5. Finally, in Section 6 we show our conclusions.

2. Observational Data

The LAMOST spectral survey provides us with a massive number of medium- ($R \sim 7{,}500$) and low-resolution ($R \sim 1{,}800$) spectra, which are collected by the innovative active reflecting Schmidt telescope located in Xinglong Observatory, China (Cui et al. 2012; Zhao et al. 2006; Deng et al. 2012). The Schmidt optics system has a large aperture (effective aperture of 3.6 m $\sim$ 4.9 m) with a wide field of view (FOV $\sim 5°$). The spectroscopic system contains 16 spectrographs with 32 integrated CCD cameras ($4K \times 4K$). A total of 4000 spectra can be obtained simultaneously via 4000 fibers plugged into the spectrographs.

Yi et al. (2014) utilized the spectra from the LAMOST pilot survey to determine the spectral subtype for 67,082 dMs by matching the relative strength of atomic and molecular features in the spectral region from 6000 to 9000 Å. Zhong et al. (2015a) classified 8639 gMs and 101,690 dMs/sdMs in LAMOST DR1 using spectral templates. Guo et al. (2015) presented a catalog of 110,321 spectra for 93,619 dMs from LAMOST DR1 and separated gMs from dMs by spectral features and 2MASS near-infrared photometry.

After the eighth year of the regular low-resolution survey, a total of 11,214,076 low-resolution spectra are available in LAMOST DR8.[5] This catalog contains 10,388,423 stellar spectra with a resolution of $R \sim 1800$ at 5500 Å, among them are 773,721 spectra from M-type stars, 520,934 of them have r-band S/N higher than 10. These spectra cover a wavelength range from 3690 to 9100 Å, including the blue channel, which is optimized for 3690–5900 Å, and the red channel, optimized for 5700–9100 Å. In this study, we adopt the identified M-type stars from LAMOST DR8 to derive the stellar parameters by applying the χ^2 minimization performed by the ULySS program.

3. Methodology

3.1. MILES Interpolator

Spectral libraries collect a set of widely used templates and corresponding stellar parameters to classify stars and synthesize stellar populations. For example, the ELODIE library (Prugniel & Soubiran 2001; Prugniel et al. 2007) contains 1962 spectra of 1070 stars obtained from the ELODIE spectrograph with a resolution of $R \sim 42{,}000$. Soubiran et al. (2008) determined the stellar parameters of ELODIE stars using the TGMET code (Katz et al. 1998). The MILES library (Sanchez-Blazquez et al. 2006; Falcón-Barroso et al. 2011) consists of 985 stars in the optical region with a resolution of $R \sim 2200$, which were obtained from the 2.5 m Isaac Newton Telescope (INT). For stars in the MILES library, Cenarro et al. (2007) compiled and calibrated stellar atmospheric parameters from the literature.

Thus, the MILES library is considered to be an ideal empirical library for stellar atmospheric parameter determination. Prugniel et al. (2011) redetermined a set of homogeneous

stellar parameters for MILES stars and built an interpolator function (version 1, hereafter V1) based on MILES spectra, which can generate model spectra based on a function of stellar parameters. The reliability of V1 has been proven as it shows better performance for both hot evolved and cool stars.

Based on V1, Sharma et al. (2016) extended the parameter space with several cool stars and refined the V1 interpolator with effective temperature downwards to 2900 K. This new interpolator[6] (version 2, hereafter V2) recalculated the stellar parameters of V1 in well-populated regions of the parameter space, while in the sparse border regions, it included external spectra for improvement. The V2 interpolator also extended the validity of M-type stars, which used a fine-tuned 26-term polynomial to improve the modeling and decrease the biases. The valid spectral range of the V2 interpolator is 3536 Å–7410 Å, which is limited by the wavelength coverage of the MILES library.

3.2. ULySS: Université de Lyon Spectroscopic Analysis Software

ULySS[7] (Koleva et al. 2009) is a full-spectrum fitting package based on the IDL/GDL language, which has been used in various types of tasks. In this work, we employ ULySS to derive the stellar atmospheric parameters by fitting a spectrum with a linear function of nonlinear models:

$$F_{\mathrm{obs}} = P_n(\lambda) \times \mathrm{TGM}(T_{\mathrm{eff}}, \log g, [\mathrm{Fe/H}], \lambda) \otimes G(v_{\mathrm{sys}}, \sigma),$$
(1)

where P_n is an nth-order polynomial, TGM represents an interpolator function modeling the spectrum with the variables denoting effective temperature, surface gravity, metallicity, and wavelength, respectively. $G(v_{\mathrm{sys}}, \sigma)$ describes the Gaussian broadening caused by the systemic velocity v_{sys} and the velocity dispersion σ. The interpolator TGM is a function of the stellar atmospheric parameters (T_{eff}, $\log g$ and [Fe/H]) and wavelength λ, providing a deduction of stellar flux distribution and χ^2 minimization.

For M-type stars, the spectra are typically occupied by dense molecular absorption bands, which make the continuum hard to determine. Because of this, we do not calculate the pseudo-continuum for normalization. Instead, we adopt a multiplicative polynomial P_n as the scaling factor, making the theoretical spectrum comparable to the observed ones. This procedure achieves the same effect as the ordinary continuum normalization. Due to the existence of molecular absorption lines, a polynomial of lower orders may not fit the features correctly, while a higher order of the multiplicative polynomial can easily overfit.

To find the best degree of polynomial P_n, we use a series of P_n with different orders in the fit procedure, calculate the loss value, then evaluate the multiple sets of results obtained. The loss value is defined as
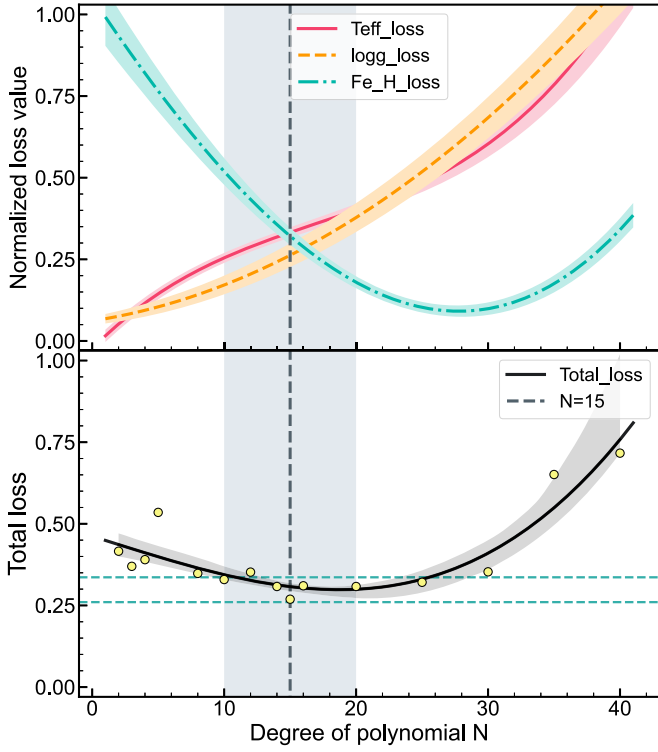
$$\mathrm{loss} = \sqrt{\sum_{i=0}^{n}(x_i - x_{\mathrm{ref}})^2}.$$
(2)

x_i represents each derived stellar parameter, and x_{ref} is the corresponding parameter provided by ASPCAP.

Figure 1. The variations of the loss value as a function of the degree of P_n. Top panel: the variation trends of the loss value for stellar parameters: $T_{\rm eff}$ (red), $\log g$ (orange), and [Fe/H] (blue) by changing the degree of the polynomial P_n. Bottom panel: the total loss value (weighted average of the three loss values above). To make the loss values of different stellar parameters comparable, each loss value is normalized to [0, 1].

To estimate the overall performance of these stellar parameters, we calculate the total loss value by performing a weighted average for the loss values of the effective temperature ($\rm loss_T$), surface gravity ($\rm loss_G$), and metallicity ($\rm loss_M$):

$$\mathrm{loss_{tot}} = \frac{w_T \times \mathrm{loss}_T + w_G \times \mathrm{loss}_G + w_M \times \mathrm{loss}_M}{w_T + w_G + w_M}. \quad (3)$$

In general, the Fe absorption lines significantly influence the determination of [Fe/H]; therefore, we decide to empirically give higher weights to [Fe/H], specifically, $w_T = 1$, $w_G = 1$, and $w_M = 1.5$.

Figure 1 shows the loss function of each stellar parameter, as well as the total loss value. The loss values of the effective temperature and surface gravity show positive correlations with the degree of polynomial P_n, while the loss value of the metallicity declines first, and then rises as the order N increases.

Eventually, we decide to adopt a maximum degree $N = 15$ for the polynomial P_n, which ensures the spectra are fitted properly and do not hit the marginal effect wall. Also, we apply the "/CLEAN" option in the ULySS program to eliminate the spikes (emission lines, bad pixels) during the fitting procedure.

After scaling the spectrum, we adopt a χ^2-minimization approach to deduce the stellar parameters. The χ^2 is defined as

$$\chi^2 = \sum_{i=1}^{n_{\rm pxl}} \left(\frac{O_i - S_i}{\sigma_i}\right)^2. \quad (4)$$

Here, $n_{\rm pxl}$ stands for the number of pixels of the spectrum, while O_i and S_i represent the flux at the ith pixel of the observed spectrum and the synthetic spectrum. The σ_i is the
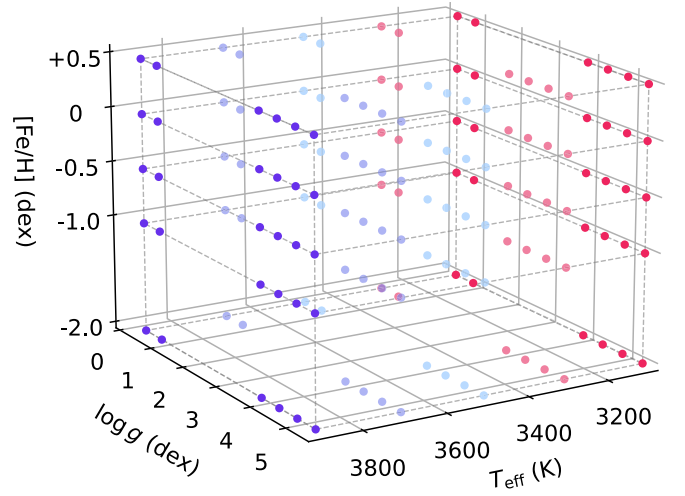
Figure 2. The initial guess values of $T_{\rm eff}$, $\log g$, and [Fe/H]. Dots are color coded in different effective temperatures. Detailed information is listed in Table 1.

Table 1
The Initial Guess Grid of Stellar Parameters

Variable	Initial Guesses					
$T_{\rm eff}$ (K)	3100	3300	3500	3700	3900	
$\log g$ (dex)	0.50	1.00	4.00	4.50	5.00	5.50
[Fe/H] (dex)	-2.00	-1.00	-0.50	0.00	0.50	

standard deviation of flux measurement at the ith pixel of the observed spectrum.

More specifically, we iteratively change the input parameters until the reduced χ^2 reaches a local minimum. The reduced χ^2 is defined as

$$\chi_\nu^2 = \frac{\chi^2}{\nu}. \quad (5)$$

Here, ν is the degree of freedom (DOF), $\nu = n_{\rm pxl} - n_{\rm para}$, which equals the difference between the number of pixels ($n_{\rm pxl}$) and the number of free parameters ($n_{\rm para}$).

Table 1 lists the initial guess grid of stellar parameters adopted in this work. It should be noted that the initial guess values provide our program with a grid of start points, and the final results are determined by the χ^2-minimization algorithm, which may exceed the grid region (see Figure 2).

In order to apply the V2 interpolator to LAMOST spectra, we have separately estimated the stellar parameters for a group of spectra by fitting the blue (3690–5700 Å) and the red (5900–9100 Å) segments of the spectra, as well as the assembled (3690–9100 Å) spectra. After a series of experiments, we found that rather than using the blue regions or the assembled spectra, fitting the red regions usually shows more robust dispersion and lower systematic error. The red segment generally has better S/N and the $\log g$-sensitive molecular bands such as TiO and CaH bands are located in this spectral region (Gizis 1997). Although some spectral signatures may be lost, we have to manually set the upper limit of our spectra as 7400 Å to avoid unreliable extrapolation. Therefore, we decide to use the overlapping parts (5700 to ~7400 Å) of the V2 spectral range and the red region of the LAMOST spectrum during the fitting.
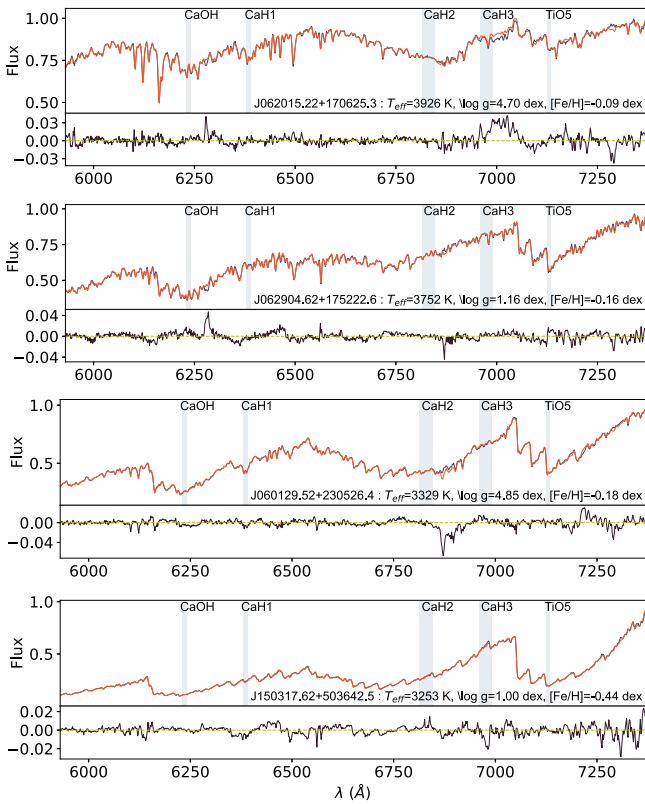
Figure 3. Samples of our fitting results with different spectral subtypes (from top to bottom: dM0, gM2, dM4, and gM6). Black and red lines are observed and model spectra, respectively. The designations and corresponding stellar parameters are listed, and the residuals between the model and observed spectra are shown at the bottom.

Finally, we construct a template-matching routine to load the observational spectrum and find the best solution by using ULySS 1.3.1 combined with the V2 interpolator. We display four samples of our fitting results with different spectral subtypes (dM0, gM2, dM4, and gM6) in Figure 3, and the residuals exhibit good consistencies in our fitting region of 5700–7400 Å. However, the fitting is not as good as the others in the spectral region near the red end, which indicates the instability of the model spectrum generation restricted by the interpolator.

4. Validation of Our Method

Before applying our method to the entire sample set, it is necessary to validate this method using a spectrum subset equipped with reliable external stellar parameters. Therefore, we crossmatch with APOGEE DR17 (Ahumada et al. 2020; Jönsson et al. 2020; Abdurro'uf et al. 2022) and 16 suitable papers from the literature, then compare the stellar parameters for the common stars.

4.1. Comparison with APOGEE DR17

We crossmatch our sample set with the APOGEE DR17 allStar-file,[8] following the criteria below:

1. $2900 < T_{\mathrm{eff}} < 4200$ K;
2. The spectral-type property in the LAMOST DR8 catalog is classified as M type by LASP;
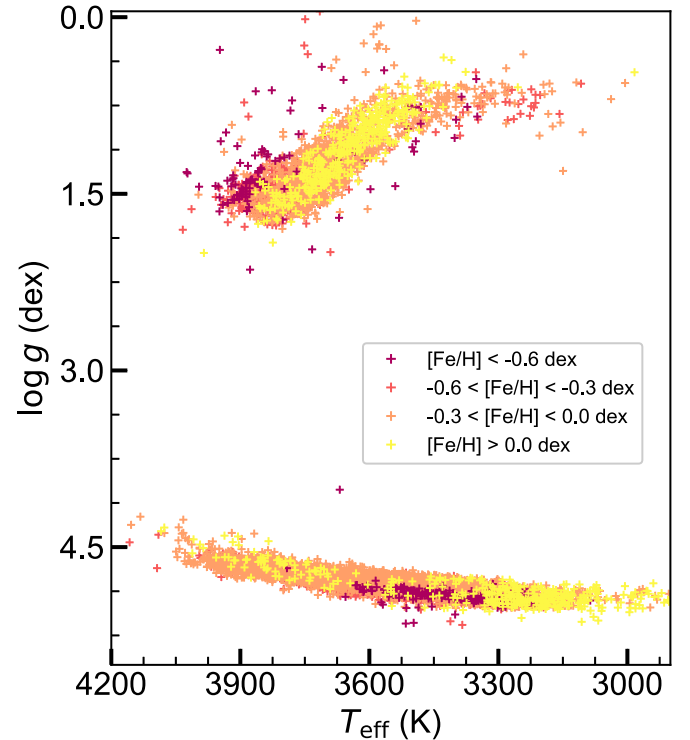
Figure 4. The distribution of T_{eff} vs. $\log g$ for common stars from APOGEE DR17. Stars are color coded in different metallicity groups.

3. The S/N of the r band (SNR_r) for the observed spectra should be larger than 20;
4. The S/N of the u, g, r, i, and z bands for the observed spectra should not equal -9999.

SNR_r is the S/N value at the SDSS r-band filter (5550–6900 Å; Gunn et al. 1998) and is defined as the median value of each pixel in this band. Note that unless specified, all S/Ns presented hereafter refer to the SNR_r value. The aim of this constraint is to ensure that our sample has good observational quality in the r-band region, which covers the distinctive spectral features. The criterion of S/N > 20 can exclude most of the misfits caused by low S/N, which will be discussed in Section 5. To avoid the influence of poor data quality, we discard the spectra whose S/N value has been artificially set as -9999 in the corresponding spectral region. In this way, we have selected 19,592 spectra of 14,532 unique stars after cross-matching. For targets with repeated observations, we only keep the spectrum with the highest S/N in order to avoid the impact of low spectral quality. Thus, we obtain a total of 14,532 common stars.

Furthermore, we exclude the binaries by crossmatching with the binary catalogs including the binaries of APOGEE (El-Badry et al. 2018), the Washington Double Star Catalog (WDS; Mason et al. 2001), the third revision of the Kepler Eclipsing Binary Catalog (KEBIII; Kirk et al. 2016), and the Gaia-ESO binary candidates (Merle et al. 2017). Similarly, we exclude the variables by crossmatching with the General Catalog of Variable Stars (GCVS; Samus' et al. 2017), the International Variable Star Index (VSX; Watson et al. 2006), and the ASAS-SN catalog of variable stars (Jayasinghe et al. 2021). After these cuts, there are 13,846 common M-type stars with APOGEE DR17. In Figure 4, we present the parameter distribution (T_{eff} versus $\log g$) of these stars.
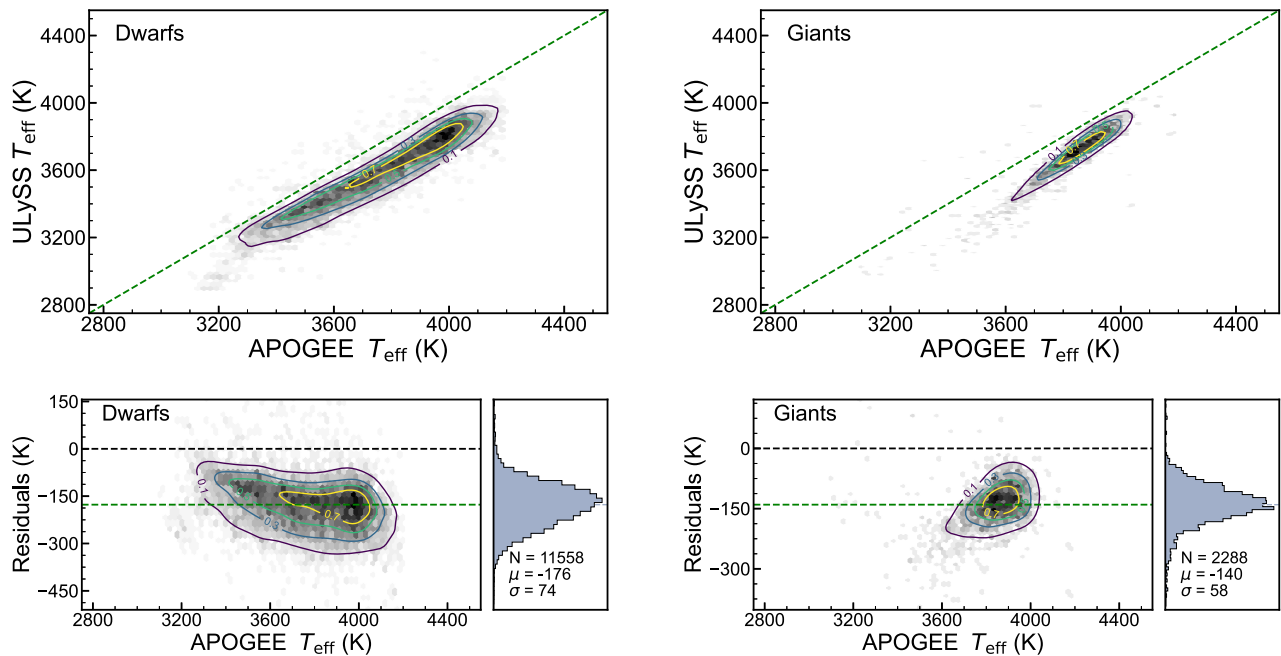
Figure 5. The comparison of the effective temperatures derived from our method with the APOGEE DR17–calibrated values. The top-left panel shows the T_{eff} comparison for dMs, while the top-right panel shows that for gMs. The bottom-left and bottom-right panels show the residuals' distributions for dMs and gMs, respectively. The color scale and the contour lines indicate the number density of each region.

As shown in Figures 5–7, the comparisons of the three stellar parameters show good agreement, although there are some systematic offsets. The bottom panels are the residuals between our results and those from APOGEE, where the mean value of the bias and the standard dispersion are also marked. The T_{eff} comparison with those of APOGEE DR17 is plotted in Figure 5, and a consistent result is found despite systematic underestimations of 176 K and 140 K for dMs and gMs, respectively. It needs to be pointed out that the APOGEE T_{eff} used in Figure 5 is calibrated by ASPCAP.[9] To illustrate the difference, we also compare with those of APOGEE spectroscopic T_{eff} in Figure A1; as a result, the systematic difference is significantly reduced to 73 K and 22 K for dMs and gMs, respectively, which suggests that there are systematic differences of T_{eff} between APOGEE and other calibrations (also reported by Birky et al. 2020).

The comparison of $\log g$ is plotted in Figure 6 for dMs and gMs. The dMs have a larger sample size, and the comparison shows good agreement for the vast majority of dMs with a small offset of 0.16 dex, while the surface gravities of gMs seem slightly overestimated with a systematic offset of 0.30 dex. The residuals generally exhibit a weak negative correlation compared to those from APOGEE—stars with higher surface gravities are underestimated, while those with lower gravities are overestimated. Similarly, the comparison with those of APOGEE spectroscopic $\log g$ is shown in Figure A2. The dispersions of both dMs and gMs are worse than the calibrated $\log g$, and the systematic difference becomes larger for dMs (0.52 dex) and slightly smaller for gMs (0.25 dex).

When comparing our [Fe/H] with those from APOGEE DR17 (see Figure 7), we find a good consistency: The systematic offsets, as well as dispersions, are 0.14 ± 0.16 dex and 0.18 ± 0.26 dex for dMs and gMs, respectively, albeit with a negative correlation in residuals.

4.2. Comparison with Other Literature

While the comparison with APOGEE DR17 has displayed the good performance of our method, we do find some systematic deviations, so it is necessary to make comparisons with other literature. Therefore, we collect stellar parameters from 16 other papers. They both worked on the stellar parameter estimation of M-type stars using different methodologies. We can take advantage of these results and make comparisons with well-determined stellar parameters.

Figure 8 displays the quantities of crossmatched stars for each literature contribution to our reference set; detailed information can be found in Table 2.

We assemble this reference set with 114,144 spectra crossmatched from those works and exclude the binary and variable candidates, similar to Section 4.1. Finally, we have 49,698 common stars in this reference set.

Figure 9 shows the parameter distribution (T_{eff} versus $\log g$) of common stars in this reference set, which displays a similar but broader parameter space compared to Figure 4.

The comparisons of these stellar parameters are presented in Figures 10–12 with the detailed offsets and standard deviations listed in the residual distributions. In Figure 10, we have compared our T_{eff} with those in the reference set, which benefits from a wide effective temperature coverage from 2900 to 4200 K. The T_{eff} offset for dMs is -88 K, which is less than the systematic offset appearing in the APOGEE comparison. For gMs, the systematic offset is -152 K, with a larger dispersion of 139 K. The differences in residual offsets also indicate a systematic difference of $\sim$100 K exists between the T_{eff} from APOGEE and those from other measurements.

In our reference set, the available $\log g$ and [Fe/H] measurements are not as large as T_{eff}; the comparisons are displayed in Figures 11 and 12. The $\log g$ for dMs derived from our method show a modest systematic offset (0.05 dex) and a good consistency compared with those from different literature.
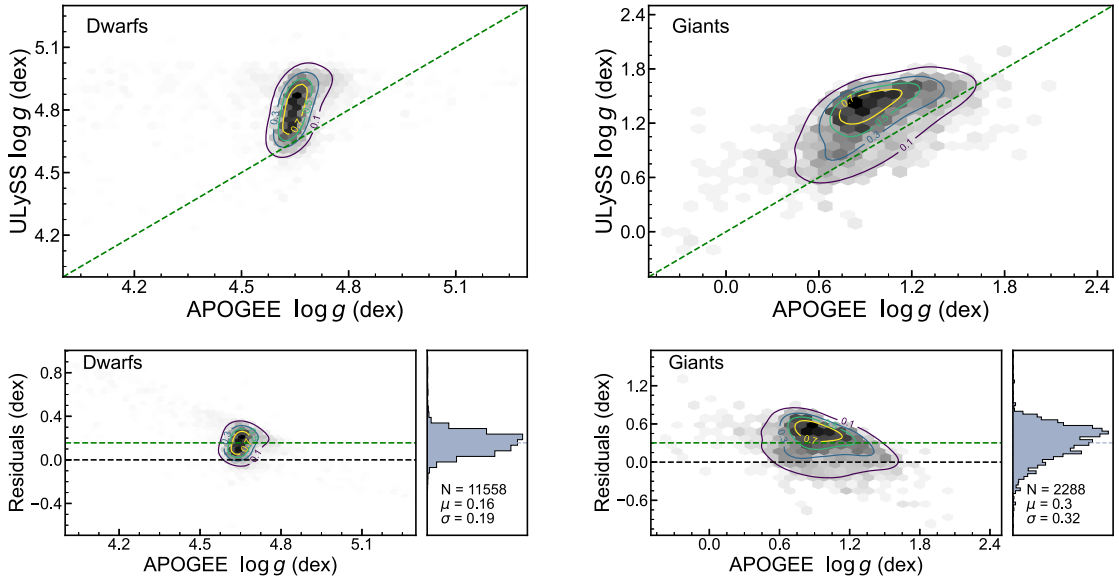
---

[9] https://dev.sdss.org/dr17/irspec/parameters/

Figure 6. Same as Figure 5, but for surface gravity.
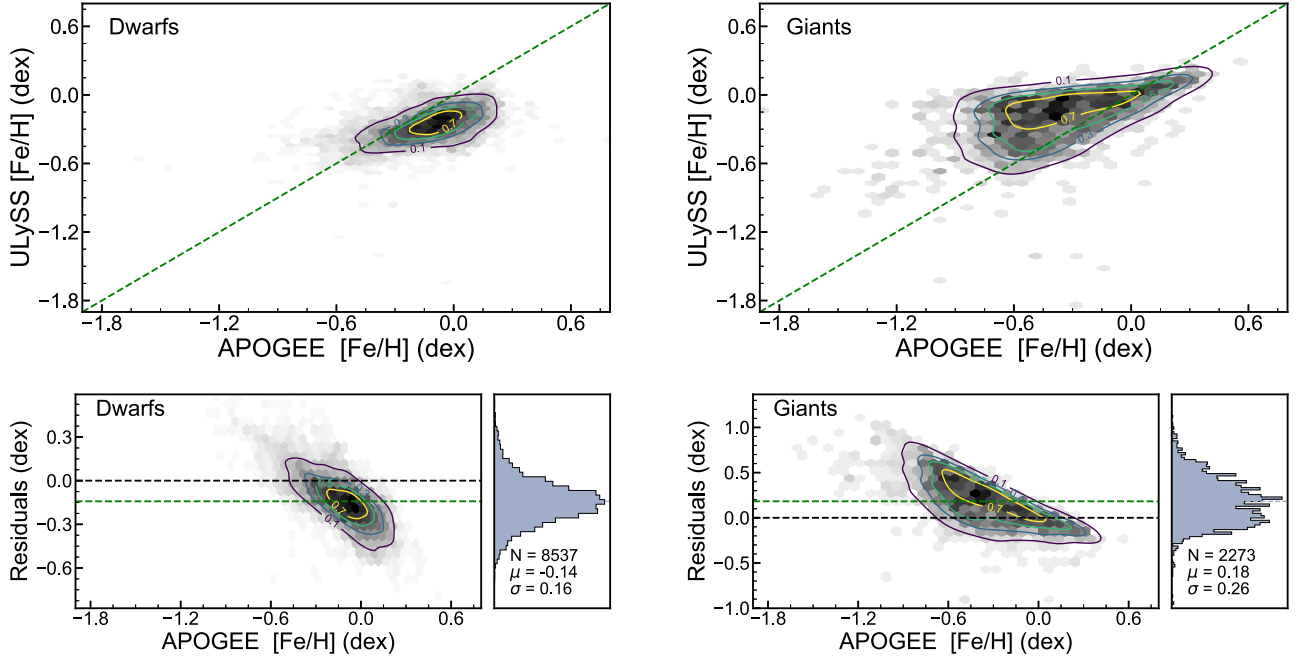

Figure 7. Same as Figure 5, but for metallicity.

For the gMs, we find a systematic offset of −0.14 dex, which is less than the offset found in the APOGEE comparison.

For [Fe/H], the residuals between our results and other measurements show a small systematic offset and dispersion, along with a weak overall decrease similar to the APOGEE comparison. The systematic offsets are −0.26 dex and 0.16 dex for dMs and gMs, respectively, which suggests that our derived [Fe/H] is generally underestimated for dMs, while the derived [Fe/H] seems overestimated for gMs.

5. Error Estimation

The comparisons in Section 4 showed that the fitting errors of our results could be influenced by stellar parameters to some

extent. Besides, the quality of the observed spectra can also affect the precision of the stellar atmospheric parameter measurement. With the help of the overlapping observations of the LAMOST survey, over 26% of stars have multiple visits in LAMOST DR8, which allows us to examine the error in stellar parameters, due to the S/N of the spectra.

In this section, we estimate the errors and investigate the precision of our measurements by comparing the stellar parameters derived from these stars with repeated observations.

5.1. Random Errors due to the Quality of Spectra

To evaluate the effect of spectral quality on the stellar parameters, we first select spectra of repeated observations for
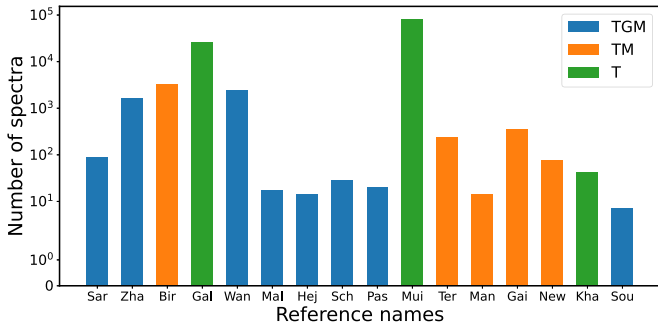
Figure 8. The number of valid stellar parameters provided by 16 papers from the literature. See Table 2 for details.

**Table 2**
Literature Sources for Comparison

Ref. Names	Common Stars	Parameters		
Sarmento et al. (2021)	91	$T_{\rm eff}$	$\log g$	[Fe/H]
Zhang et al. (2021)	1579	$T_{\rm eff}$	$\log g$	[Fe/H]
Birky et al. (2020)	3047	$T_{\rm eff}$	...	[Fe/H]
Galgano et al. (2020)	26,502	$T_{\rm eff}$	...	...
Wang et al. (2020)	2284	$T_{\rm eff}$	$\log g$	[Fe/H]
Maldonado et al. (2020)	17	$T_{\rm eff}$	$\log g$	[Fe/H]
Hejazi et al. (2020)	14	$T_{\rm eff}$	$\log g$	[Fe/H]
Schweitzer et al. (2019)	28	$T_{\rm eff}$	$\log g$	[Fe/H]
Passegger et al. (2018)	20	$T_{\rm eff}$	$\log g$	[Fe/H]
Muirhead et al. (2018)	79,658	$T_{\rm eff}$	...	...
Terrien et al. (2015)	237	$T_{\rm eff}$	...	[Fe/H]
Mann et al. (2015)	14	$T_{\rm eff}$	...	[Fe/H]
Gaidos et al. (2014)	355	$T_{\rm eff}$	...	[Fe/H]
Newton et al. (2014)	1192	$T_{\rm eff}$	...	[Fe/H]
Khata et al. (2021)	43	$T_{\rm eff}$	...	...
Souto et al. (2021)	7	$T_{\rm eff}$	$\log g$	[Fe/H]

the same stars, with a difference in S/N that should be lower than 20%. Figure 13 shows the residuals of stellar parameters for these duplicate stars as a function of S/N. We use the standard dispersion to represent the errors of stellar parameter determination, which present decreasing tendencies as the S/N of spectra increase. We split our sample into dMs (top panel) and gMs (bottom panel), as well as grouped stars into different temperature bins.

The effective temperatures are less sensitive to S/N. Generally, the cooler stars tend to have better precision, except for the coolest stars ($T_{\rm eff} < 3000$ K), and there are not as many stars as other groups in our sample set. For the spectra of S/N ~ 5, the precision of $T_{\rm eff}$ is better than 120 K, and it immediately decays to 45 K when S/N is higher than 20.

However, the surface gravities are very sensitive to the S/N of spectra, which may be due to the molecular bands blurred by noise. For both dMs and gMs, $\log g$ can be determined with a precision better than 0.2 dex for S/N > 20. For the low-S/N spectra, the measurement of $\log g$ is visually poor, e.g., the dispersion of hot dwarfs ($T_{\rm eff} > 3900$ K) can be as large as 0.85 dex, which becomes the main reason to exclude them from our comparisons.

A similar situation can be found for metallicities, which show a significant dependence on S/N. In general, dMs can have more precise [Fe/H] than gMs. For dMs in each temperature group, the precision of [Fe/H] is about 0.24 dex when the S/N is about 5 and rapidly decreases to 0.08 dex
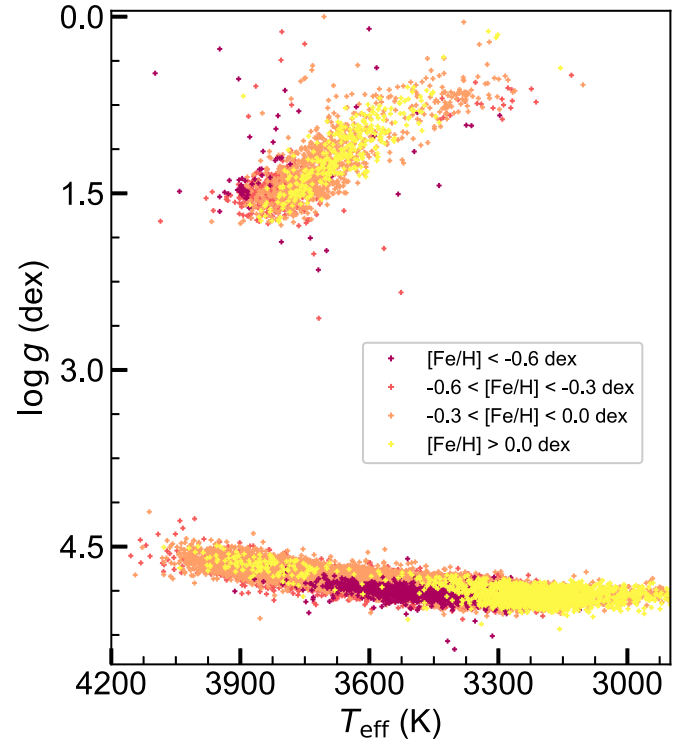
Figure 9. The distribution of $T_{\rm eff}$ vs. $\log g$ for common stars from the reference set. Stars are color coded in different metallicity groups.

when the S/N reaches 15. The determination of [Fe/H] for gMs is relatively poor as the precision reaches 0.36 dex of S/N ~ 5 and 0.2 dex of S/N > 25, respectively. In each temperature group, the [Fe/H] dispersion for gMs differs from the other groups, indicating a dependence of the [Fe/H] determination on $T_{\rm eff}$.

### 5.2. Systematic Errors due to S/N

Furthermore, in order to investigate the possible systematic errors introduced by low spectral quality, we select spectra of repeated observations for the same targets with different S/N, of which the spectra with higher S/N should be 40 times higher than the spectra of low S/N. The residuals are represented by $\Delta P = P_{\rm high} - P_{\rm low}$, where P refers to the three stellar parameters, $P_{\rm high}$ stands for that with the higher S/N, while $P_{\rm low}$ is for the one with a lower S/N.

Figure 14 exhibits the difference between stellar parameters deduced from spectra of repeated observations as a function of lower S/N. The asymmetry of residual distributions indicates that systematic deviations exist between high- and low-S/N results.

We use error bars to present the standard dispersion of each S/N bin and perform linear regressions of mean values in each bin (see the yellow dashed lines in Figure 14) to generalize the gradients of systematic deviations for $T_{\rm eff}$, $\log g$, and [Fe/H]. Similarly, $T_{\rm eff}$ shows good precision and is less sensitive to the S/N of lower spectral quality and can be determined with a systematic difference better than 50 K at S/N ~ 10. The systematic errors of $\log g$ are quite obvious in the low-S/N region, which indicates that surface gravities deduced from low-S/N spectra are systematically underestimated compared to those from high S/N. It should be noted that, for some stars of S/N lower than 5, the differences between surface gravities
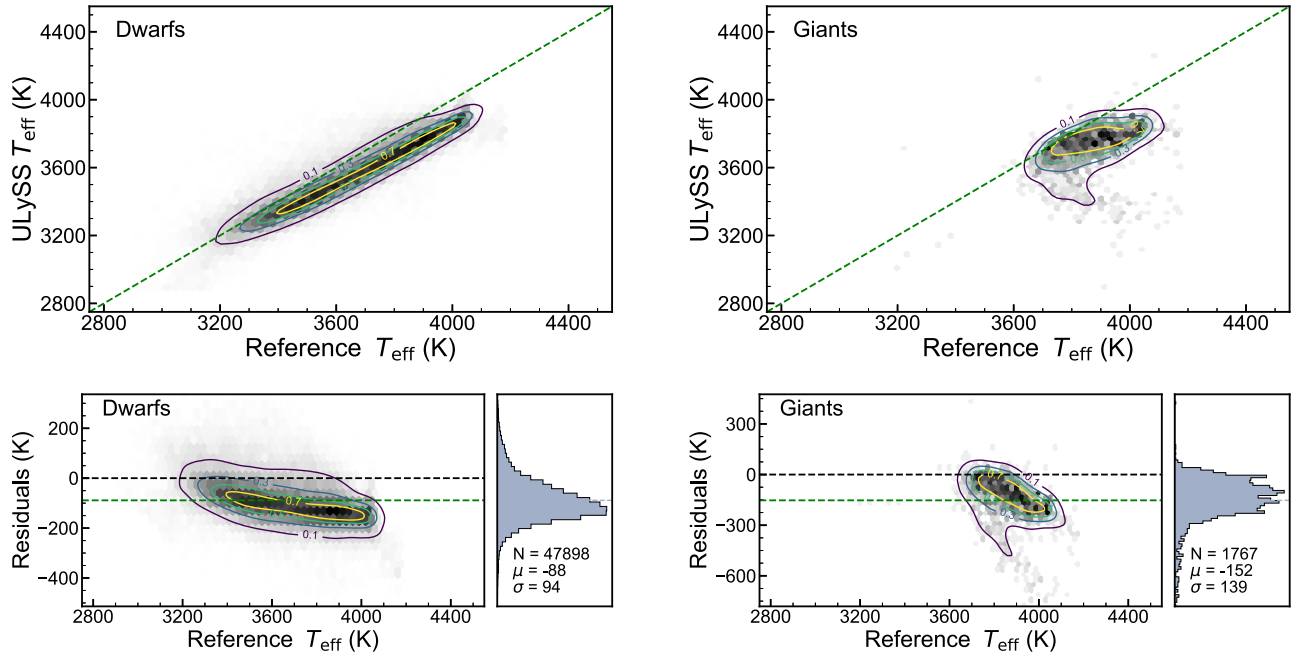
Figure 10. The comparison of the effective temperatures derived from our method with the literature values. The top-left panel shows the T_{eff} comparison for dMs, while the top-right panel for gMs. The bottom-left and bottom-right panels show the residuals' distributions for dMs and gMs, respectively. The color scale and the contour lines indicate the number density of each region.
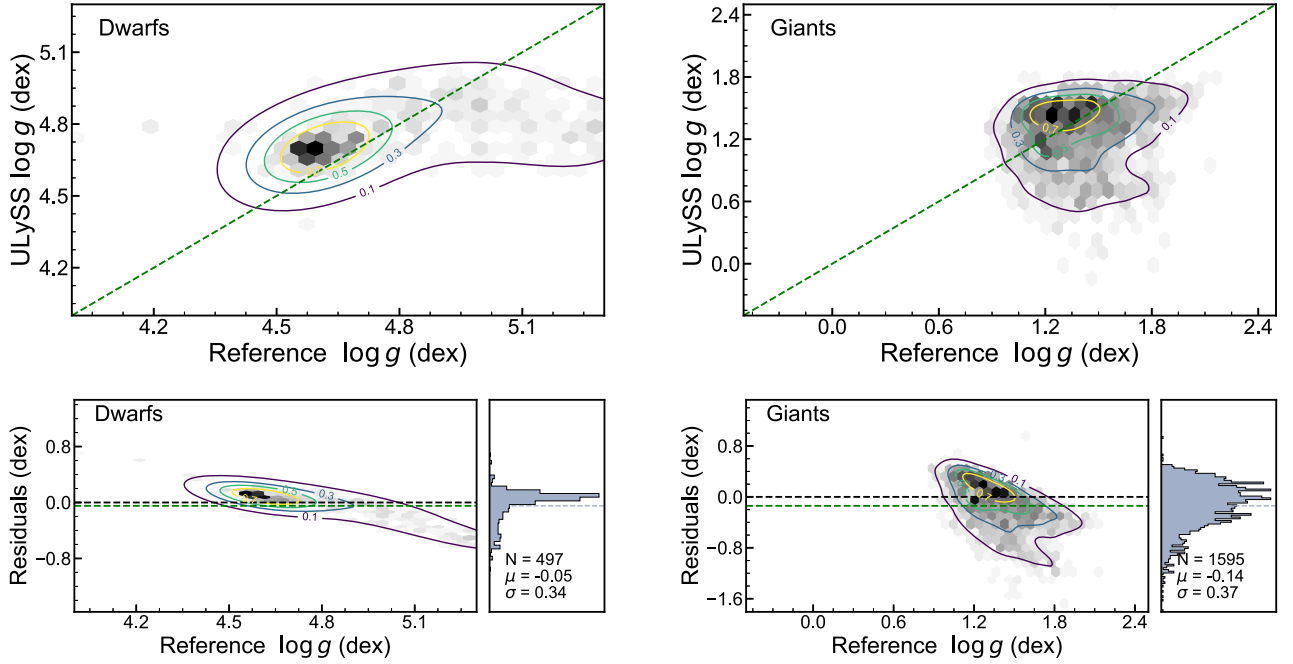
Figure 11. Same as Figure 10, but for surface gravity.

derived from high- and low-S/N spectra can be as bad as $\sim$2.5 dex, which suggests that our program tends to misclassify some dMs as gMs in the low-S/N region. For [Fe/H], an obvious underestimation of $\sim$0.7 dex appears at S/N $\sim$ 5; however, for sample stars with S/N higher than 20, the systematic errors are less than 0.2 dex, which is less significant.

5.3. Internal Uncertainty Analysis

As we know, during the χ^2 minimization, errors can be introduced by the fitting procedure. We evaluate the internal

uncertainties of our stellar parameter measurements in three steps. In the first step, we sample a set of stellar parameters (2900–4500 K for T_{eff}, 0.0–6.0 dex for $\log g$, and -2.5 to $+1.0$ dex for [Fe/H]) based on their distribution in the stellar parameter space of our results. Second, we utilize these stellar parameters to obtain the corresponding spectra generated from the V2 interpolator and add Gaussian noises to simulate the distortion during observations. In the third step, we redetermine the stellar parameters for all these generated spectra from a single Markov Chain Monte Carlo (MCMC) simulation. We
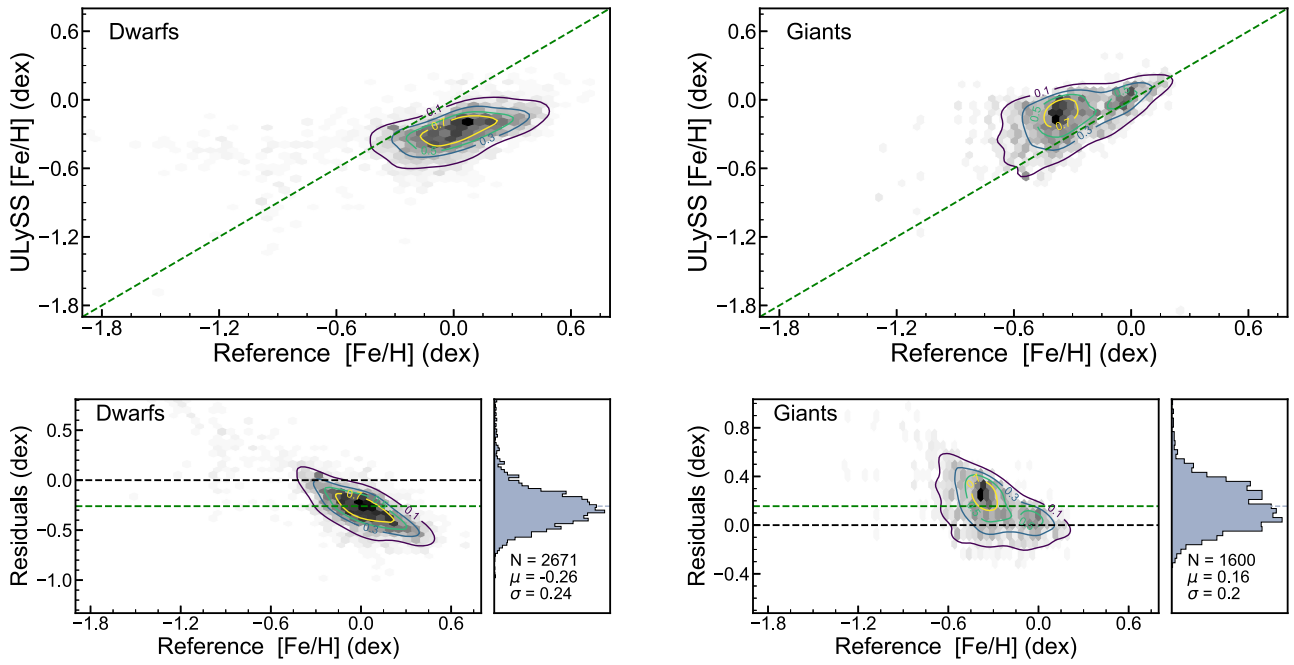
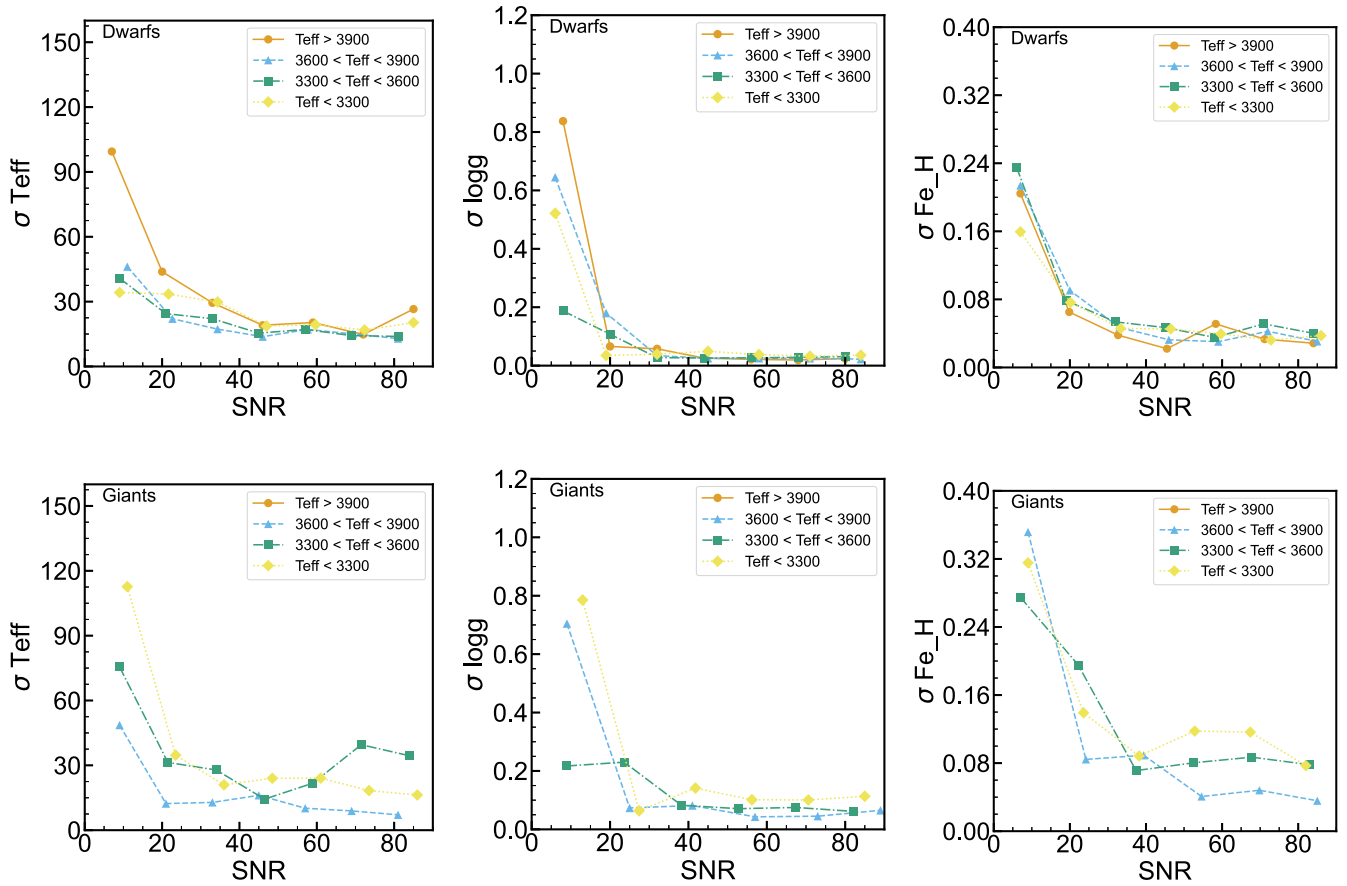**Figure 12.** Same as Figure 10, but for metallicity.

Figure 13. The random errors of stellar parameters as functions of S/N. The dMs (top) and gMs (bottom) are grouped into different temperature bins. The dots represent the standard dispersion in each S/N bin.

calculate the residuals between the input stellar parameters in step 1 and the outputs in step 3 and present the deviations of these residuals in Figure 15.

We notice that hot metal-poor giants generally have worse performance than the others, especially in the low-S/N region. For spectra of S/N > 20, stellar parameters can be determined
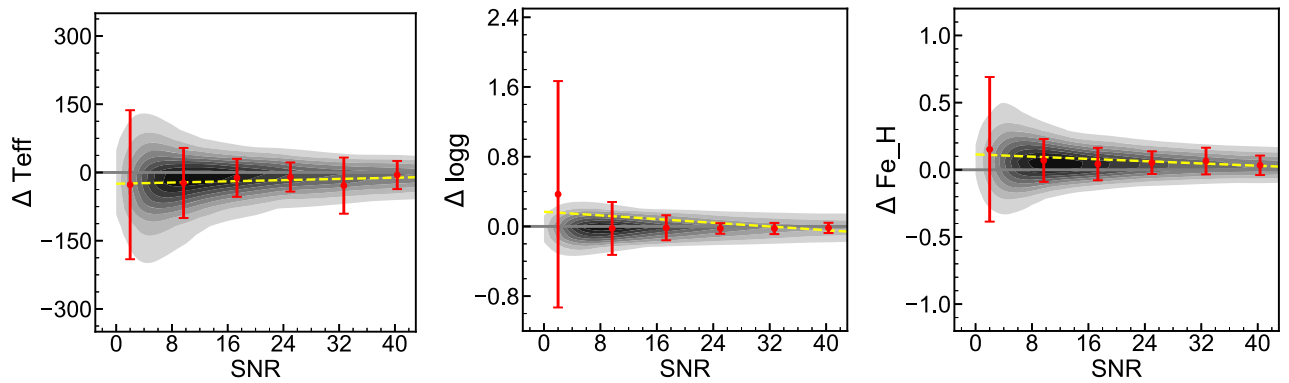
Figure 14. The systematic errors of stellar parameters as functions of the S/N. Red error bars represent the standard deviations in each S/N bin, and the red dots in the center are the means. The yellow dashed lines are linear regressions of the means.
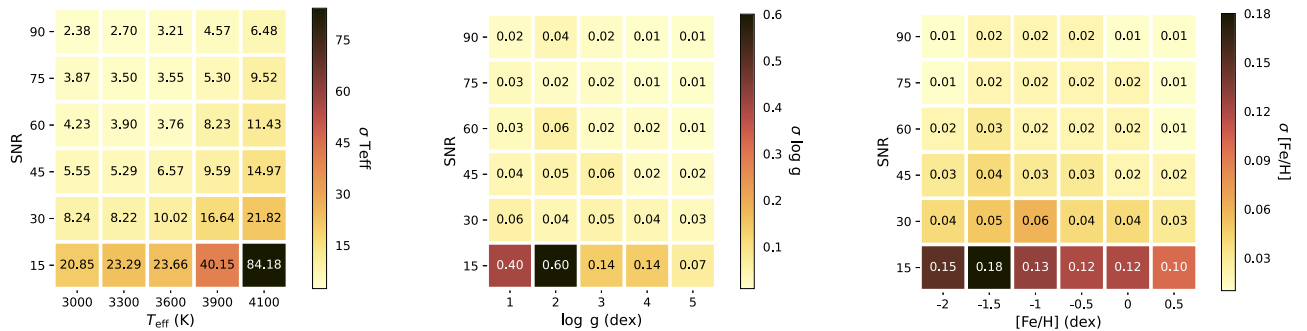

Figure 15. The internal uncertainties in different stellar parameters and S/N values. The values in each box stand for the standard deviation of residuals within each interval.

with internal uncertainties better than 22 K, 0.06 dex, and 0.06 dex for $T_{\rm eff}$, $\log g$, and [Fe/H], respectively. It should be noted that the error obtained in this simulation is lower than those in the external comparisons because the theoretical spectrum with randomly added noise is more ideal than the observed spectrum.

5.4. The Catalog of Stellar Atmospheric Parameters

We present the stellar atmospheric parameter catalog of our results, which contains 763,136 spectra of 616,314 M-type stars from LAMOST LRS DR8. In Table B1, we show a sample set of our stellar parameter results and several important attributes, including the celestial coordinates, spectral quality information: S/N in the u, g, r, and i bands as well as the spectral identification information: the LAMOST designation (desig), LAMOST unique spectra ID (obsid), and the source identifier (source_id) from Gaia Early Data Release 3 (Collaboration et al. 2021).

In Figure 16, we present the distribution of S/Ns for the observational spectra. Spectra with S/N below 20 account for more than half of our samples; one should be careful using their stellar parameters. As discussed in Section 5, we recommend using the stellar parameters derived from spectra with S/N higher than 20 for reliability and good consistency. Additionally, in Figure 17, we plot the results derived from our method along with theoretical isochrones from the PAdova and TRieste Stellar Evolution Code (PARSEC; Bressan et al. 2012) for stars with S/N above 20 and below 20. As illustrated in the top panel, the stars of metallicity above the solar value ([Fe/H] > 0.0 dex) can be clearly distinguished via the
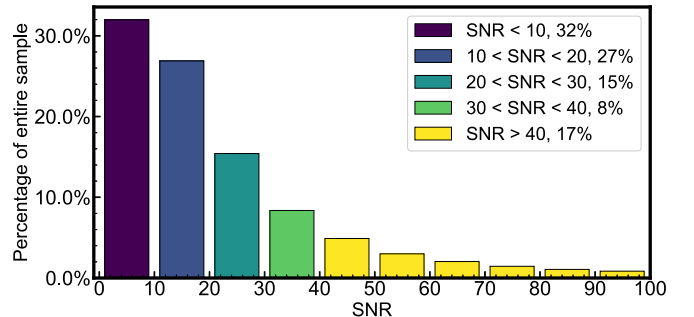

Figure 16. The percentage for the stars with S/N below 10, from 10 to 20, 20 to 30, 30 to 40, and above 40.

isochrone. Moreover, the comparison between the top and bottom panels shows the improvement of the S/N cut discussed above. Conspicuous outliers are rare for stars of S/N > 20.

We note that the lower limit of derived $T_{\rm eff}$ is as low as 2900 K. For gMs, the lower limit of $\log g$ can reach -0.24 dex, and for dMs, the upper limit is 5.9 dex. Figure 18 displays the distributions of [Fe/H] values for dMs and gMs, separately. The dMs show a more symmetrical distribution with a peak [Fe/H] around -0.30 dex. For gMs, however, the peak is more skewed toward solar abundance.

5.5. Potential Future Uses

This work builds on a number of other parameter determination studies for cool stars. Our study provides a significantly larger sample than the current literature sources
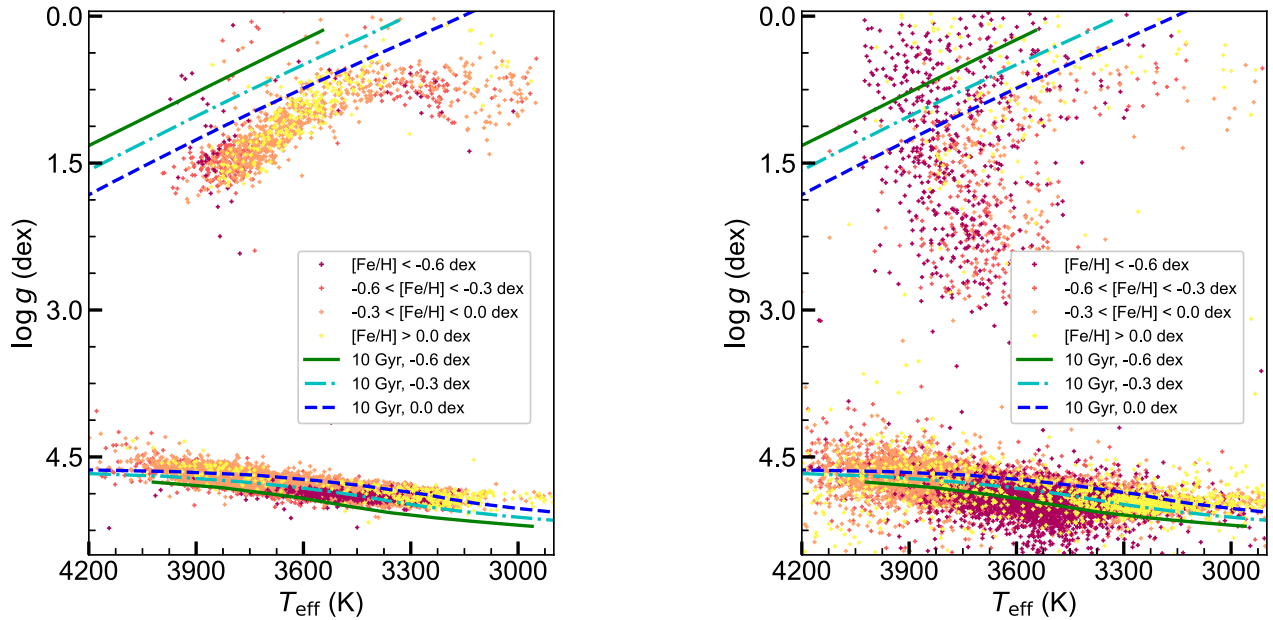
Figure 17. Left panel: the Kiel diagram colored by different metallicity groups of the samples with S/N > 20. Lines correspond to 10 Gyr PARSEC isochrones with [Fe/H] = −0.6, −0.3, and 0.0 dex, respectively. Right panel: the same Kiel diagram but for stars of S/N < 20.
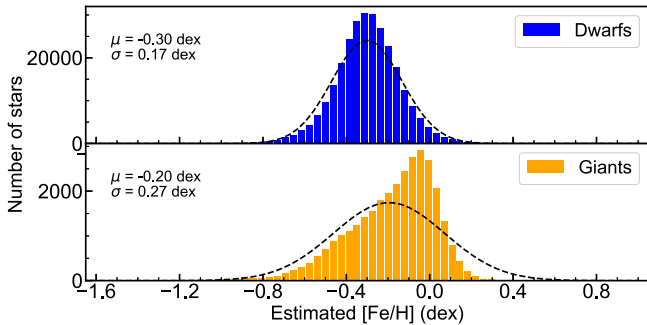
Figure 18. The histograms of [Fe/H] for dMs (top panel) and gMs (bottom panel). The histograms only display the [Fe/H] range from −1.6 dex to 1.0 dex, as there are only a few metal-poor stars ([Fe/H] < −1.6 dex).

that we have presented detailed comparisons in Table 2. This allows our catalog to provide well-characterized properties which might be useful for a wide range of purposes. Objects that are found to be time-variable in some way greatly benefit from having known properties. These properties of cool stars may help with the immediate interpretation or prove valuable for further follow-up studies. These might be individual systems that are for example found to host a planet or perhaps stars where an asteroseismic analysis enables the identification of interesting oscillation modes. These two use cases are also appropriate for the case of larger samples. It might be interesting to look at planetary formation as a function of metallicity (e.g., Lu et al. 2020), or metallicity might be related to asteroseismic evolutionary information for large numbers of stars (e.g., Bellinger et al. 2019).

Our catalog can also be valuable as a means to recognize important outliers among the two key populations of cool stars: the most numerous stars (dMs) and most luminous stars (gMs). Such studies can provide valuable insights for understanding and modeling the evolution of both stellar properties as well as inferences about our galaxy and beyond. The properties of cool stars with age can provide a range of different information useful in a range of contexts. The slow evolution of dMs provides the most pristine view of elements unchanged by their lack of evolution through only a small fraction of their main-sequence lifetime (e.g., Laughlin et al. 1997). On the other hand, gMs are useful probes of the mixing of evolved stars as well as dust. It is not clear that these are fully consistent with the predictions of stellar evolutionary models (e.g., Lançon et al. 2018). Such efforts together underpin systematic empirical grids of stellar types, which are in turn a vital component of galaxy evolution models. It has long been known that the detailed properties of gMs on the horizontal branch as a function of stellar properties are vital (e.g., Worthey 1994; Cabrera-Ziri & Conroy 2022) though dMs can also dominate the energy output of galaxies (e.g., Conroy & van Dokkum 2012; van Dokkum & Conroy 2021). In the era of Gaia parameters, large-scale spectroscopic properties from surveys such as LAMOST can be key in a detailed modern understanding of our galaxy. Our future work includes repeat observations, examination, and determinations of our sample to further enhance our robust characterization of the properties of M stars.

6. Conclusion

Utilizing the MILES V2 interpolator and ULySS, we derive the stellar atmospheric parameters for 763,136 spectra of 616,314 M-type stars from LAMOST DR8. We compare our stellar parameters with external references including APOGEE DR17 and other literature, and good consistency can be found. To evaluate the precision of our results, we analyze the stars with repeated observations. The precision of the derived stellar parameters is mainly dependent on the S/N and effective temperature. For S/N higher than 20, the typical precisions are better than 45 K, 0.25 dex, and 0.22 dex for T_{eff}, $\log g$, and [Fe/H], respectively. A Monte Carlo simulation is applied to check the performance of our method, and the internal uncertainty

of our method is $\sigma_{T_{eff}} <$ 22 K, $\sigma_{\log g} <$ 0.06 dex, and $\sigma_{[Fe/H]} <$ 0.06 dex for spectra with S/N better than 20.

Our results supply LAMOST LRS DR8 with large numbers of well-determined stellar atmospheric parameters of M-type stars, and our method could be applied to works on stellar parameter determination for M-type stars in future low-resolution surveys, for example, LAMOST LRS DR9. More-over, it is important to further investigate the metallicity distributions and kinematic properties of different Galactic populations.

Appendix A
Appendix Figures

We find some systematic offsets between the stellar parameters derived from our method and the APOGEE-calibrated values. However, those systematic offsets are less significant when we comparing with the APOGEE spectro-scopic values in Figures A1 and A2.
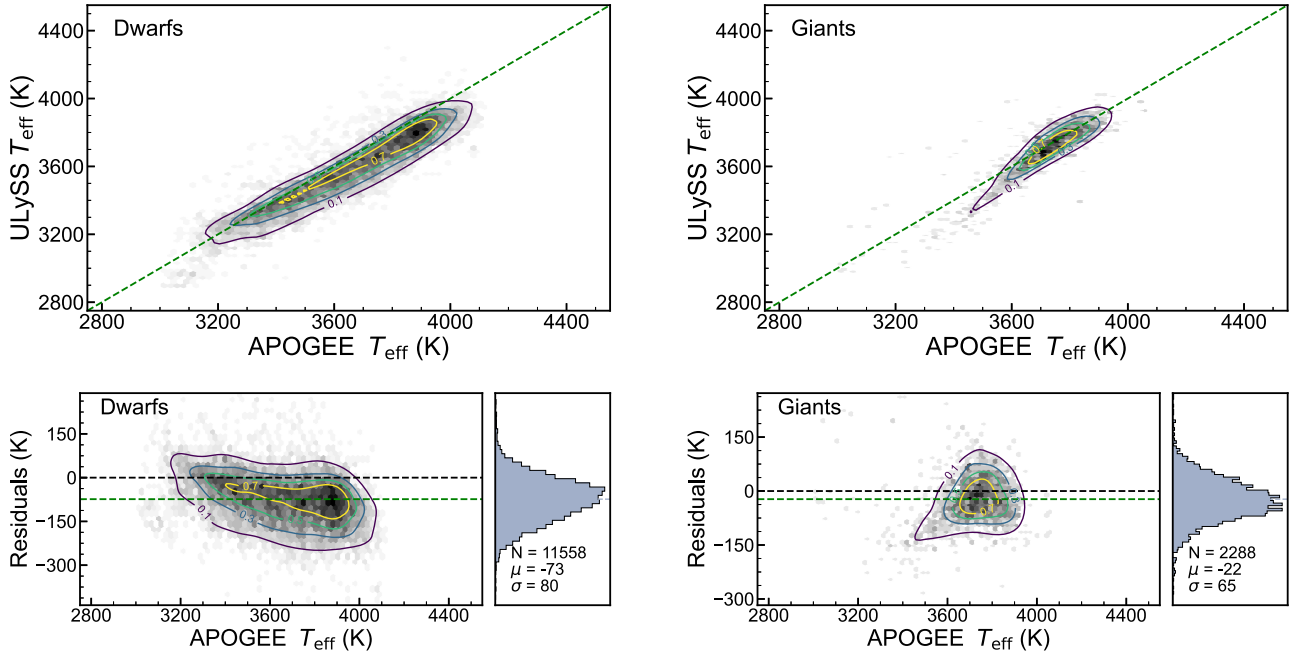
Figure A1. The comparison of the effective temperatures derived from our method with the APOGEE DR17 spectroscopic values. The top-left panel shows the T_{eff} comparison for dMs, while the top-right panel is for gMs. The bottom-left and bottom-right panels show the residuals' distributions for dMs and gMs, respectively. The color scale, as well as the contour lines, indicates the number density of each region.
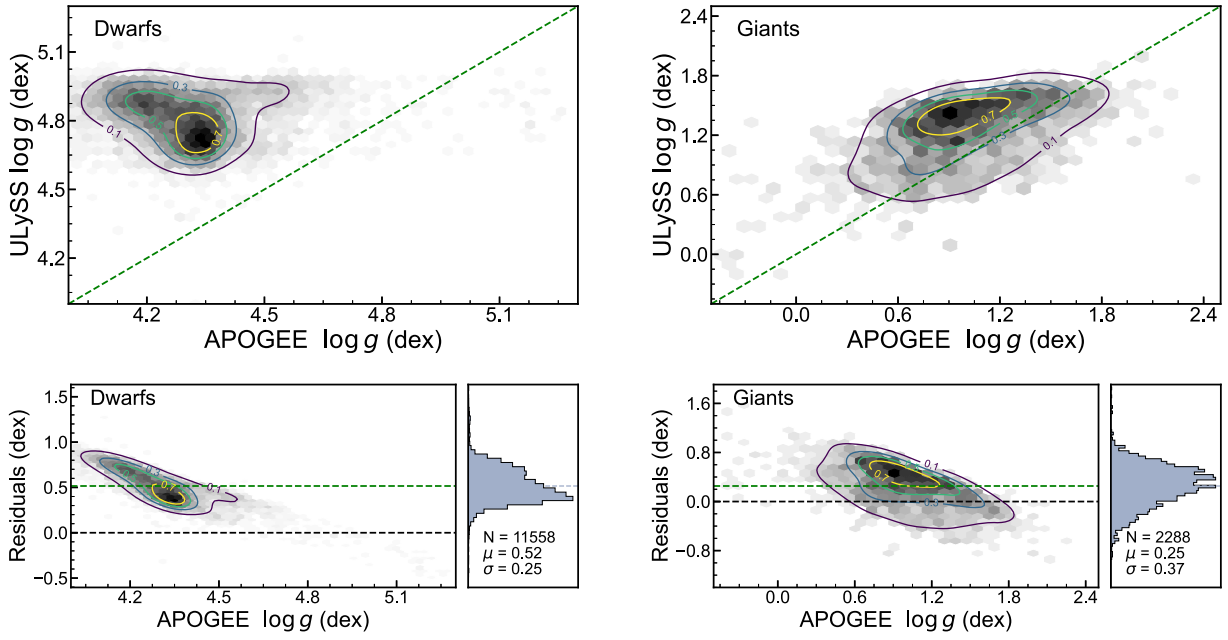
Figure A2. Same as Figure A1, but for surface gravity.

Appendix B
Appendix Table

We present the stellar atmospheric parameters of M-type stars from LAMOST LRS DR8 in Table B1.

Table B1
Stellar Parameters of Randomly Selected Objects

desig	obsid	source_id	R.A. hms (J2000)	Decl. dms (J2000)	SNR_r	RV (km s^{-1})	T_eff (K)	log g (dex)	[Fe/H] (dex)
J003233.56+023235.4	182907177	2547554358360573184	00:32:33.57	+02:32:35.4	21	−0.6	3865	4.66	−0.23
J005018.74+383849.1	407239	367934386366947456	00:50:18.75	+38:38:49.1	12	−38.7	3699	4.73	−0.11
J005137.86+382236.2	612710127	367725002416518272	00:51:37.87	+38:22:36.3	35	−20.0	3739	4.73	−0.40
J062058.46+210949.0	437312190	3375942048114941696	04:11:37.63	+33:59:16.6	144	−26.4	3409	0.52	−0.11
J041137.62+335916.6	200512017	170751686193676288	06:14:31.81	+08:40:37.2	46	−63.6	3755	2.39	−0.64
J061431.80+084037.2	503710146	3328420434007985280	06:20:58.46	+21:09:49.0	22	1.9	3506	1.58	−0.52
J063953.53+534915.5	546315051	994279332683432320	06:39:53.54	+53:49:15.5	14	−23.7	3782	1.46	−0.47
J065018.79+264542.8	46204100	3385128472059867904	06:50:18.80	+26:45:42.8	20	−33.3	3907	4.64	−0.21
J071141.54+195445.8	175006180	3363557565751137152	07:11:41.54	+19:54:45.9	42	−32.5	3813	4.63	−0.16
J082845.70+104545.1	337405103	600889912104424192	08:28:45.71	+10:45:45.1	49	15.5	3915	4.65	−0.15
J085752.81+155051.6	629901215	610580732712396032	08:57:52.82	+15:50:51.6	67	27.7	3657	4.89	−0.45
J103456.90−054946.3	422001160	3777400028612544640	10: 4:56.91	−05:49:46.3	17	−52.6	3947	4.67	−0.38
J104029.59+040235.2	546101111	3857828655644765440	10:40:29.60	+04:02:35.2	15	53.0	3970	4.50	−0.11
J143657.78+285648.1	566705048	1281154251515481344	14:36:57.78	+28:56:48.2	29	−8.8	3792	4.75	−0.37
J143700.28+313008.0	319815214	1286110746854188288	14:37:00.29	+31:30:08.0	32	14.3	3765	4.73	−0.29
J144136.81+162250.9	450707153	1234646382833797632	14:41:36.81	+16:22:50.9	17	−52.4	3574	4.85	−0.40
J144852.72−001936.8	649007156	3650703754716377344	14:48:52.46	−00:19:36.9	209	50.1	3045	0.68	−0.09
J235515.89+042523.8	505908050	2743370468663782528	23:55:15.90	+04:25:23.9	20	23.5	3791	4.58	−0.25

Note. The attribute column is not fully presented here. The complete catalog is accessible in its entirety in a machine-readable format.

(This table is available in its entirety in machine-readable form.)

ORCID iDs

Ming-Yi Ding ⓘ https://orcid.org/0000-0001-6898-7620
Jian-Rong Shi ⓘ https://orcid.org/0000-0002-0349-7839
Hugh R. A. Jones ⓘ https://orcid.org/0000-0003-0433-3665
Hong-Liang Yan ⓘ https://orcid.org/0000-0002-8609-3599
Chun-Qian Li ⓘ https://orcid.org/0000-0002-6647-3957
Qi Gao ⓘ https://orcid.org/0000-0003-4972-0677
Tian-Yi Chen ⓘ https://orcid.org/0000-0002-6448-8995
Jing-Hua Zhang ⓘ https://orcid.org/0000-0002-2510-6931
Shuai Liu ⓘ https://orcid.org/0000-0001-5193-1727
Tai-Sheng Yan ⓘ https://orcid.org/0000-0003-2318-9013

References

Abdurro'uf, Accetta, K., Aerts, C., et al. 2022, ApJS, 259, 35
Ahumada, R., Prieto, C. A., Almeida, A., et al. 2020, ApJS, 249, 3
Allard, F., Homeier, D., & Freytag, B. 2011, in ASP Conf. Ser. 448, The 16th Cambridge Workshop on Cool Stars, Stellar Systems and the Sun (San Francisco, CA: ASP), 91
Allard, F., Homeier, D., & Freytag, B. 2012, RSPTA, 370, 2765
Allard, F., Homeier, D., Freytag, B., et al. 2013, MSAIS, 24, 128
Bellinger, E. P., Hekker, S., Angelou, G. C., Stokholm, A., & Basu, S. 2019, A&A, 622, A130
Bessell, M. S. 1991, AJ, 101, 662
Birky, J., Hogg, D. W., Mann, A. W., & Burgasser, A. 2020, ApJ, 892, 31
Bonfils, X., Delfosse, X., Udry, S., et al. 2013, A&A, 549, A109
Bressan, A., Marigo, P., Girardi, L., et al. 2012, MNRAS, 427, 127
Brown, A. G. A., Vallenari, A., Prusti, T., et al. 2018, A&A, 616, A1
Cabrera-Ziri, I., & Conroy, C. 2022, MNRAS, 511, 341
Casey, A. R., Hogg, D. W., Ness, M., et al. 2016, arXiv:1603.03040
Cenarro, A. J., Gorgas, J., Cardiel, N., et al. 2001, MNRAS, 326, 981
Cenarro, A. J., Peletier, R. F., Sanchez-Blazquez, P., et al. 2007, MNRAS, 374, 664
Conroy, C., & van Dokkum, P. 2012, ApJ, 747, 69
Cui, X.-Q., Zhao, Y.-H., Chu, Y.-Q., et al. 2012, RAA, 12, 1197
De Silva, G. M., Freeman, K. C., Bland-Hawthorn, J., et al. 2015, MNRAS, 449, 2604
Deng, L.-C., Newberg, H. J., Liu, C., et al. 2012, RAA, 12, 735
Eisenstein, D. J., Weinberg, D. H., Agol, E., et al. 2011, AJ, 142, 72
El-Badry, K., Ting, Y.-S., Rix, H.-W., et al. 2018, MNRAS, 476, 528
Falcón-Barroso, J., Sánchez-Blázquez, P., Vazdekis, A., et al. 2011, A&A, 532, A95
Gaia Collaboration, Brown, A. G. A., Vallenari, A., et al. 2021, A&A, 650, C3
Gaidos, E., Mann, A. W., Lépine, S., et al. 2014, MNRAS, 443, 2561
Galgano, B., Stassun, K., & Rojas-Ayala, B. 2020, AJ, 159, 193
García Pérez, A. E., Prieto, C. A., Holtzman, J. A., et al. 2016, AJ, 151, 144
Gizis, J. E. 1997, AJ, 113, 806
Gray, R. O., & Corbally, J. 2009, Stellar Spectral Classification (Princeton, NJ: Princeton Univ. Press)
Gunn, J. E., Carr, M., Rockosi, C., et al. 1998, AJ, 116, 3040
Gunn, J. E., Siegmund, W. A., Mannery, E. J., et al. 2006, AJ, 131, 2332
Guo, Y.-X., Yi, Z.-P., Luo, A.-L., et al. 2015, RAA, 15, 1182
Gustafsson, B., Edvardsson, B., Eriksson, K., et al. 2008, A&A, 486, 951
Hejazi, N., Lépine, S., Homeier, D., Michael Rich, R., & Shara, M. M. 2020, AJ, 159, 30
Ho, A. Y. Q., Ness, M. K., Hogg, D. W., et al. 2017, ApJ, 836, 5
Husser, T.-O., Wende-von Berg, S., Dreizler, S., et al. 2013, A&A, 553, A6
Jayasinghe, T., Kochanek, C. S., Stanek, K. Z., et al. 2021, MNRAS, 503, 200
Jofré, P., Heiter, U., & Soubiran, C. 2019, ARA&A, 57, 571
Jönsson, H., Holtzman, J. A., Prieto, C. A., et al. 2020, AJ, 160, 120
Katz, D., Soubiran, C., Cayrel, R., Adda, M., & Cautain, R. 1998, A&A, 338, 151
Kesseli, A. Y., Davy Kirkpatrick, J., Fajardo-Acosta, S. B., et al. 2019, AJ, 157, 63
Khata, D., Mondal, S., Das, R., & Baug, T. 2021, MNRAS, 507, 1869
Kirk, B., Conroy, K., Prša, A., et al. 2016, AJ, 151, 68

Kirkpatrick, J. D. 1992, PhD thesis, The Univ. of Arizona
Kirkpatrick, J. D., Reid, I. N., Liebert, J., et al. 1999, ApJ, 519, 802
Koleva, M., Prugniel, P., Bouchard, A., & Wu, Y. 2009, A&A, 501, 1269
Lançon, A., Gonneau, A., Trager, S. C., et al. 2018, arXiv:1811.02841
Laughlin, G., Bodenheimer, P., & Adams, F. C. 1997, ApJ, 482, 420
Le Borgne, J.-F., Bruzual, G., Pelló, R., et al. 2003, A&A, 402, 433
Lepine, S., Rich, R. M., & Shara, M. M. 2007, ApJ, 669, 1235
Li, J., Liu, C., Zhang, B., et al. 2021, ApJS, 253, 45
Liu, C., Fu, J., Shi, J., et al. 2020, arXiv:2005.07210
Lu, C. X., Schlaufman, K. C., & Cheng, S. 2020, AJ, 160, 253
Luo, A.-L., Zhao, Y.-H., Zhao, G., et al. 2015, RAA, 15, 1095
Majewski, S. R., Schiavon, R. P., Frinchaboy, P. M., et al. 2017, AJ, 154, 94
Maldonado, J., Micela, G., Baratella, M., et al. 2020, A&A, 644, A68
Mann, A. W., Feiden, G. A., Gaidos, E., Boyajian, T., & von Braun, K. 2015, ApJ, 804, 64
Mann, A. W., Gaidos, E., Lépine, S., & Hilton, E. J. 2012, ApJ, 753, 90
Mason, B. D., Wycoff, G. L., Hartkopf, W. I., Douglass, G. G., & Worley, C. E. 2001, AJ, 122, 3466
Merle, T., Eck, S. V., Jorissen, A., et al. 2017, A&A, 608, A95
Muirhead, P. S., Dressing, C. D., Mann, A. W., et al. 2018, AJ, 155, 180
Ness, M., Hogg, D. W., Rix, H.-W., Ho, A. Y. Q., & Zasowski, G. 2015, ApJ, 808, 16
Newton, E. R., Charbonneau, D., Irwin, J., et al. 2014, AJ, 147, 20
Passegger, V. M., Reiners, A., Jeffers, S. V., et al. 2018, A&A, 615, A6
Passegger, V. M., Bello-García, A., Ordieres-Meré, J., et al. 2020, A&A, 642, A22
Prugniel, P., & Soubiran, C. 2001, A&A, 369, 1048
Prugniel, P., Soubiran, C., Koleva, M., & Borgne, D. L. 2007, arXiv:astro-ph/0703658
Prugniel, P., Vauglin, I., & Koleva, M. 2011, A&A, 531, A165
Quirrenbach, A., , CARMENES Consortium, Amado, P. J., et al. 2020, Proc. SPIE, 11447, 114473C
Rajpurohit, A. S., Allard, F., Rajpurohit, S., et al. 2018, A&A, 620, A180
Reid, I. N., Hawley, S. L., & Gizis, J. E. 1995, AJ, 110, 1838
Reiners, A., Zechmeister, M., Caballero, J. A., et al. 2018, A&A, 612, A49
Samus', N. N., Kazarovets, E. V., Durlevich, O. V., Kireeva, N. N., & Pastukhova, E. N. 2017, ARep, 61, 80
Sanchez-Blazquez, P., Peletier, R. F., Jimenez-Vicente, J., et al. 2006, MNRAS, 371, 703
Sarmento, P., Rojas-Ayala, B., Mena, E. D., & Blanco-Cuaresma, S. 2021, A&A, 649, A147
Schweitzer, A., Passegger, V. M., Cifuentes, C., et al. 2019, A&A, 625, A68
Sharma, K., Prugniel, P., & Singh, H. P. 2016, A&A, 585, A64
Smola, A. J., & Schölkopf, B. 2004, Stat. Comput., 14, 199
Soubiran, C., Bienaymé, O., Mishenina, T. V., & Kovtyukh, V. V. 2008, A&A, 480, 91
Souto, D., Cunha, K., & Smith, V. V. 2021, ApJ, 917, 11
Steinmetz, M., Zwitter, T., Siebert, A., et al. 2006, AJ, 132, 1645
Terrien, R. C., Mahadevan, S., Deshpande, R., & Bender, C. F. 2015, ApJS, 220, 16
Ting, Y.-S., Conroy, C., Rix, H.-W., & Cargile, P. 2019, ApJ, 879, 69
Valdes, F., Gupta, R., Rose, J. A., Singh, H. P., & Bell, D. J. 2004, ApJS, 152, 251
van Dokkum, P., & Conroy, C. 2021, ApJ, 923, 43
Wang, R., Luo, A.-L., Chen, J.-J., et al. 2020, ApJ, 891, 23
Watson, C. L., Henden, A. A., & Price, A. 2006, in Society for Astronomical Sciences 25th Annual Symp. on Telescope Science (Ranco Cucamonga, CA: Society for Astronomical Sciences), 47
Worthey, G. 1994, ApJS, 95, 107
Wu, Y., Luo, A.-L., Li, H.-N., et al. 2011, RAA, 11, 924
Xiang, M. S., Liu, X. W., Yuan, H. B., et al. 2015, MNRAS, 448, 822
Yee, S. W., Petigura, E. A., & von Braun, K. 2017, ApJ, 836, 77
Yi, Z., Luo, A., Song, Y., et al. 2014, AJ, 147, 33
Zhang, B., Liu, C., & Deng, L.-C. 2020, ApJS, 246, 9
Zhang, S., Luo, A.-L., Comte, G., et al. 2019, ApJS, 240, 31
Zhang, S., Luo, A.-L., Comte, G., et al. 2021, ApJ, 908, 131
Zhao, G., Chen, Y.-Q., Shi, J.-R., et al. 2006, ChJAA, 6, 265
Zhong, J., Lépine, S., Li, J., et al. 2015a, RAA, 15, 1154
Zhong, J., Lépine, S., Hou, J., et al. 2015b, AJ, 150, 42